

# Bubble Dynamics with Phase Change near a Compliant Object

M. Rodriguez Jr.<sup>1</sup>, S. H. Bryngelson<sup>2</sup>, T. Colonius<sup>3</sup>  
(<sup>1</sup>Brown University, <sup>2</sup>Georgia Institute of Technology,  
<sup>3</sup>California Institute of Technology, USA)

## ABSTRACT

Cavitation near rigid and compliant surfaces leads to damage to naval structures. Phase change is involved in the nucleation, growth, and collapse of bubbles but is often ignored in interface-capturing simulations of multiphase flows. Near-surface bubble collapses and phase change have been studied independently. Still, the importance of phase change during these bubble oscillations and collapses and how this relates to the impact loads at the surface remains unknown. We use the open-source Multi-component Flow Code (MFC), a fully Eulerian framework, to access these scales and model phase change. The Eulerian six-equation multiphase physical and numerical model uses an interface- and shock-capturing approach. Phase change is modeled as a kinetic process involving volume, thermal, and mass transfer at the interface. The numerical implementation is verified using 1D cavitation and shock tube problems and a two-phase relaxation solver with finite relaxation. We then study an underwater explosion cavitation bubble problem near a rigid wall and a rigid wall with an elastomeric coating. The sharp drop of pressure from the rarefaction wave in the wake of the underwater explosion cavitates the liquid near the boundary. We study the dependence of initial bubble stand-off distance from the nearby surface and pressure on the maximum wall pressures and water vapor mass production. The coating inhibits the phase change and reduces the pressure loading experienced at the rigid wall compared to the no-coating case.

## 1 INTRODUCTION

The explosive growth and violent bubble collapse during cavitation damages nearby rigid and compliant surfaces (e.g., elastomeric coatings). During operation, negative transient pressures in the flow vaporize the liquid water, and small vapor bubbles grow rapidly and collapse near structural surfaces. The adjacent rigid or coated surface is subjected to successive cavitation-induced pitting that

limits the structural life cycle (Blake and Gibson, 1987; Franc et al., 2011; Kim et al., 2014). During the vaporization, energy may be released into the surroundings as a shock as the vapor and gas bubble undergoes explosive growth. Both the underwater explosion event and shock can damage nearby surfaces. Upon reaching its maximum volume, the bubble is out of equilibrium with its surroundings due to the pressure imbalance between the internal bubble gas contents and the surrounding liquid. The bubble collapses, converting the liquid potential energy to kinetic energy. The bubble concentrates the kinetic energy and implodes, releasing an outward-propagating shock wave capable of damaging surrounding surfaces (Rayleigh, 1917; Benjamin and Ellis, 1966).

Nearby surfaces or objects break the spherical symmetry of an exploding and collapsing bubble. Underwater explosion experiments by Cole (1948) showed the scaling relation of the max (peak) pressure as a function of distance from the explosion. The peak pressure scaling is a linearly inverse relationship with  $p_{\max} \propto \gamma_o^{-1.13}$ , where  $\gamma_o$  is the initial stand-off radial distance from explosion and the additional 0.13 decay in the exponent is attributed to the energy necessary to sustain the shock. Similarly, the non-spherical dynamics of collapsing bubbles have been extensively examined (Kornfeld and Suvorov, 1944; Lauterborn and Bolle, 1975; Blake and Gibson, 1987). Unlike the spherical collapse (idealized implosion), the pressures produced on the surface are attributed to a water-hammer shock wave emitted from a re-entrant jet impinging upon the opposite side of the bubble (Naude and Ellis, 1961; Plesset and Chapman, 1971) or directly on the solid surface (Tomita and Shima, 1986). Moreover, using a combination of theory and empirical observations, Supponen et al. (2016, 2017) developed scaling relationships for the re-entrant jet speeds as functions of driving pressure and initial bubble stand-off distance from the nearby wall. However, experimental investigation of bubble and wave dynamics in configurations involving surfaces/compliant objects is challenging due to limited optical access and the wide

range of spatio-temporal scales.

Numerical simulation approaches have been used to predict explosive bubble growth and collapse. These simulations complement these investigations and enable predictions of the wall impacts loads in bubble explosion and implosion problems. Utilizing the incompressible or weakly compressible liquid assumption, boundary element, and boundary integral methods (Blake et al., 1986; Aganin et al., 2016; Brujan et al., 2019) and potential flow calculations (Plesset and Chapman, 1971; Molefe and Peters, 2019) can simulate single bubble collapse near a wall morphology, re-entrant jet speeds, and material pitting (Hsiao et al., 2014). However, such approaches cannot capture wave-wall interactions pertinent to cavitation damage and subsequent inception with high-fidelity. For this purpose, interface-capturing methods are advantageous for resolving compressible flows and obeying the conservation laws (Shyue, 1998; Saurel and Abgrall, 1999; Abgrall, 1996). The interface-capturing numerical approach typically solves the five-equation multiphase model (Allaire et al., 2002; Kapila et al., 2001; Perigaud and Saurel, 2005; Murrone and Guillard, 2005; Shukla et al., 2010) which is a single velocity and energy equation reduced model of the seven-equation multiphase model of Baer and Nunziato (1986). The five-equation multiphase model has been used for underwater explosion (UNDEX) (Nguyen et al., 2021; Phan et al., 2021) and bubble collapse (Johnsen and Colonius, 2009; Beig et al., 2018; Tiwari et al., 2013) studies. One disadvantage of such an approach is the diffused representation of material interfaces across  $\sim 3$ -4 computational cells. Higher-order accurate numerical methods, e.g., Weighted Essentially Non-Oscillatory (WENO) methods (Jiang and Shu, 1996), are then used to capture nonlinear (high-frequency content) waves (e.g., shocks) and maintain sharp material interfaces for high-fidelity bubble dynamic simulations in a liquid (Johnsen and Colonius, 2006; Beig and Johnsen, 2015; Coralic and Colonius, 2013) and near surfaces (Rodriguez, 2018).

We augment the open-source Multi-component Flow Code (MFC), a fully Eulerian framework using a high-order accurate, shock- and interface-capturing numerical solver (Bryngelson et al., 2020; Coralic and Colonius, 2013), to include phase change to investigate single bubble growth dynamics near a compliant object. MFC simulates 3D fluid-structure interaction and multi-scale cavitation problems (Trummel et al., 2020; Schmidmayer et al., 2020b). Coupled evolution equations for the linear elastic contribution to the Cauchy stress tensor account for the model material elasticity (Rodriguez and Johnsen, 2019). We use the six-equation multiphase model (Saurel et al., 2009) extended to model phase change as a kinetic process (thermal and mass transfer) (Saurel et al., 2008; Pelanti and Shyue, 2014) that

takes place at gas/liquid interfaces. The model considers pressure-, thermal-, and chemical-disequilibrium at a phase interface of the same substance (e.g., liquid water and water vapor) and assumes that the thermodynamic equilibrium is achieved infinitely fast. We implement the multi-component six-equation multiphase approach of Pelanti and Shyue (2019) and associated infinite relaxation procedures into MFC to study UNDEX problems near an elastomeric coating. This proceeding is outlined as follows. The physical and numerical models for multiphase and multi-component flows are presented in §2. In §3, 1D cavitation- and shock-tube test problems are presented. We then study the wave dynamics, water vapor production, and maximum wall pressures of two-dimensional axisymmetric UNDEX bubble growth and collapse numerical simulations near a rigid wall and a rigid wall with an elastomeric coating. We summarize our findings in §4.

## 2 PHYSICAL & NUMERICAL MODELS

### 2.1 GOVERNING EQUATIONS

The six-equation, single-velocity compressible multiphase flow model, is considered (Saurel and Abgrall, 1999; Zein et al., 2010; Pelanti and Shyue, 2014). Phase change is modeled as a kinetic process involving thermal and mass transfer at the interface (Saurel et al., 2008) and assumed to reach equilibrium infinitely fast. The model is extended to multi-components with the first two phases undergoing phase change (Pelanti and Shyue, 2019). We consider the governing equations based on the phase internal energy formulation:

$$\partial_t \alpha_k + \mathbf{u} \cdot \nabla \alpha_k = \sum_{j=1}^N \mathcal{P}_{kj}, \quad k = 1, 2, \dots, N \quad (1a)$$

$$\partial_t (\alpha_1 \rho_1) + \nabla \cdot (\alpha_1 \rho_1 \mathbf{u}) = \mathcal{M}, \quad (1b)$$

$$\partial_t (\alpha_2 \rho_2) + \nabla \cdot (\alpha_2 \rho_2 \mathbf{u}) = -\mathcal{M}, \quad (1c)$$

$$\partial_t (\alpha_k \rho_k) + \nabla \cdot (\alpha_k \rho_k \mathbf{u}) = 0, \quad k = 3, \dots, N, \quad (1d)$$

$$\partial_t (\rho \mathbf{u}) + \nabla \cdot \left[ \rho \mathbf{u} \otimes \mathbf{u} + \left( \sum_{k=1}^N \alpha_k p_k \right) \mathbb{I} \right] = 0, \quad (1e)$$

$$\begin{aligned} \partial_t (\alpha_1 \mathcal{E}_1) + \nabla \cdot (\alpha_1 (\mathcal{E}_1 + p_1) \mathbf{u}) = \\ - \sum_{j=1}^N p_{11j} \mathcal{P}_{1j} + \sum_{j=1}^N \mathcal{Q}_{1j} + g_1 \mathcal{M}, \end{aligned} \quad (1f)$$

$$\begin{aligned} \partial_t (\alpha_2 \mathcal{E}_2) + \nabla \cdot (\alpha_2 (\mathcal{E}_2 + p_2) \mathbf{u}) = \\ - \sum_{j=1}^N p_{12j} \mathcal{P}_{2j} + \sum_{j=1}^N \mathcal{Q}_{2j} - g_1 \mathcal{M}, \end{aligned} \quad (1g)$$

$$\partial_t (\alpha_k \mathcal{E}_k) + \nabla \cdot (\alpha_k (\mathcal{E}_k + p_k) \mathbf{u}) = - \sum_{j=1}^N p_{Ijk} \mathcal{P}_{kj} + \sum_{j=1}^N \mathcal{Q}_{kj}, \quad k = 3, \dots, N, \quad (1h)$$

where  $\rho_k$ ,  $\alpha_k$ ,  $p_k$ , and  $\mathcal{E}_k$  are the phase  $k$  density, volume fraction, and specific internal energy per unit volume, respectively. The velocity vector and identity tensors are denoted  $\mathbf{u}$  and  $\mathbb{I}$ , respectively. The mixture relations are  $\sum_k \alpha_k = 1$  and  $\sum_k \rho_k \alpha_k = \rho$ , where  $\rho$  is the mixture density and specific volume is  $v$ . The mixture internal energy per unit volume is  $\mathcal{E} = \sum_k \alpha_k \mathcal{E}_k$ . The total energy per unit volume  $E$  is the sum internal and kinetic:  $E = \mathcal{E} + \frac{1}{2} \rho u_k^2$ . For numerical stability (Schmidmayer et al., 2020a), the total energy is numerical conserved by solving the additional equation,

$$\partial_t E + \nabla \cdot ((E + p) \mathbf{u}) = 0. \quad (2)$$

The terms  $\mathcal{P}_{kj}$  and  $\mathcal{Q}_{kj}$  represent the volume transfer (pressure disequilibrium) and heat transfer, respectively. The term  $\mathcal{M}$  is the mass transfer between phases 1 and 2, the liquid and vapor phases, respectively. These transfer terms are defined as

$$\begin{aligned} \mathcal{P}_{kj} &= \mu_{kj}(p_k - p_j), \quad \mathcal{Q}_{kj} = \theta_{kj}(T_j - T_k), \\ \mathcal{M} &= \nu(g_2 - g_1), \end{aligned} \quad (3)$$

where  $T_k$  denotes the temperature and  $g_k$  the Gibbs free energy (chemical potential) of phase  $k$ . The mechanical, thermal, and chemical relaxation parameters follow the following relation  $\phi_{kj} = \phi_{jk} \geq 0$ ,  $\phi_{kk} = 0$ , and  $\phi_{ij} = -\phi_{ji}$ . While there is no physical significance to these parameters, they are related to the rate of relaxation (Pelanti and Shyue, 2014). The terms  $p_{Ijk} = p_{Ikj}$  and  $g_I$  are the interfacial pressures and chemical potential, respectively. The mechanical relaxation is assumed to take place infinitely fast for all phases throughout the computational domain, i.e.,  $\mu_{kj} = \mu_{jk} \rightarrow \infty$  (Saurel et al., 2008; Pelanti and Shyue, 2019). The parameters  $\mu_{jk}$ ,  $\theta_{jk}$ , and  $\nu$  are assumed to be infinite near the interface and zero elsewhere such that,

$$\mu_{jk}, \theta_{jk} = \begin{cases} \infty & \text{if } \epsilon \leq \alpha_k \leq 1 - \epsilon, \\ 0 & \text{otherwise,} \end{cases} \quad (4a)$$

$$\nu = \begin{cases} \infty & \text{if } \epsilon \leq \alpha_k \leq 1 - \epsilon \text{ and } T_{\text{liq}} > T_{\text{sat}}, \\ 0 & \text{otherwise,} \end{cases} \quad (4b)$$

where  $\epsilon$  defines the liquid-vapor interface, set to  $\epsilon = 10^{-6}$  (see Saurel et al. (2008)).

Eq. (1) is regarded as the parent model for multiphase equations modeling phase change as a kinetic process. By activating different relaxation effects, a hierarchy of multiphase governing equations was shown by Pelanti and Shyue (2019) along with the associated speeds of

sound calculations. For brevity, we summarize the hierarchy of governing equations and expand on the numerical method to achieve infinitely fast relaxation in §2.3.2. The simplest disequilibrium model assumes instantaneous mechanical (pressure) relaxation and is referred to as the  $p$ -Relaxed model. The next model in the hierarchy assumes instantaneous mechanical and thermal relaxation for all phases and is referred to as the  $pT$ -Relaxed model. Finally, the  $pTg$ -Relaxed model assumes instantaneous mechanical and thermal relaxation for all phases and chemical relaxation for the first two phases. We note that the six-equation model is a generalization of reduced five-equation of Kapila et al. (2001).

## 2.2 EQUATION OF STATE

To close system (1), the Stiffened Gas Equation of State (SG EoS) of Le Métayer et al. (2004) is used to relate the mixture internal energy to pressure and temperature, respectively:

$$\rho e = p \sum_k \frac{\alpha_k}{n_k - 1} + \sum_k \alpha_k \frac{n_k B_k}{n_k - 1} + \sum_k \rho_k \alpha_k q_k, \quad (5a)$$

$$\rho e = T \sum_k \rho_k \alpha_k c_{v,k} + \sum_k \alpha_k B_k + \sum_k \rho_k \alpha_k q_k, \quad (5b)$$

where  $T$  is the temperature and  $q_k$ ,  $n_k$ ,  $B_k$ , and  $c_{v,k}$  are material properties prescribed to produce the correct propagation speeds in liquids and solids (Harlow and Amsden, 1971; Le Métayer et al., 2005). The phase entropy and Gibbs free energy are defined as (Le Métayer et al., 2005),

$$s_k = c_{v,k} \ln \left( \frac{T_k^{n_k}}{(p_k + B_k)^{n_k - 1}} \right) + \eta_k, \quad (6)$$

$$\begin{aligned} g_k &= (n_k c_{v,k} - \eta_k) T_k - \\ &c_{v,k} T_k \ln \left( \frac{T_k^{n_k}}{(p_k + B_k)^{n_k - 1}} \right) + q_k, \end{aligned} \quad (7)$$

respectively, where  $\eta_k$  is SG EoS constant evaluated at a reference entropy, pressure, and temperature (e.g., saturation conditions at room temperature). Table 1 tabulates the material constants for the water. The mixture speed of sound is  $a = \sum_k \sqrt{Y_k a_k^2}$  where  $Y_k = \rho_k \alpha_k / \rho$  and  $a_k = \sqrt{n_k(p + B_k) / \rho_k}$  are the phase mass fraction and speed of sound, respectively.

## 2.3 NUMERICAL METHOD

The open-source Multi-component Flow Code (MFC) (Bryngelson et al., 2020) is used to solve Eq. (1). To describe the MFC numerical implementation, we recast the Eq. (1) in vector notation

$$\partial_t \mathbf{q} + \nabla \cdot \mathbf{F}(\mathbf{q}) + \mathbf{h}(\mathbf{q}) \nabla \cdot \mathbf{u} = \mathbf{r}_\mu(\mathbf{q}) + \mathbf{r}_\theta(\mathbf{q}) + \mathbf{r}_\nu(\mathbf{q}), \quad (8)$$

where  $\mathbf{q}$  is the state vector,  $\mathbf{F}$  the flux tensor, and  $\mathbf{h}$  the non-conservative term. The right-hand-side terms  $\mathbf{r}_\mu$ ,  $\mathbf{r}_\theta$ , and  $\mathbf{r}_\nu$  are the mechanical, thermal and chemical relaxation terms, respectively. The vectors are defined as

$$\mathbf{q} = \begin{bmatrix} \alpha_1 \\ \alpha_2 \\ \vdots \\ \alpha_N \\ \alpha_1 \rho_1 \\ \alpha_2 \rho_2 \\ \vdots \\ \alpha_N \rho_N \\ \rho \mathbf{u} \\ \alpha_1 \mathcal{E}_1 \\ \alpha_2 \mathcal{E}_2 \\ \vdots \\ \alpha_N \mathcal{E}_N \end{bmatrix}, \quad \mathbf{F} = \begin{bmatrix} \alpha_1 \mathbf{u} \\ \alpha_2 \mathbf{u} \\ \vdots \\ \alpha_N \mathbf{u} \\ \alpha_1 \rho_1 \mathbf{u} \\ \alpha_2 \rho_2 \mathbf{u} \\ \vdots \\ \alpha_N \rho_N \mathbf{u} \\ \rho \mathbf{u} \otimes \mathbf{u} + \sum_{k=1}^N \alpha_k p_k \mathbb{I} \\ \alpha_1 \mathcal{E}_1 \mathbf{u} \\ \alpha_2 \mathcal{E}_2 \mathbf{u} \\ \vdots \\ \alpha_N \mathcal{E}_N \mathbf{u} \end{bmatrix}, \quad (9a)$$

$$\mathbf{h} = \begin{bmatrix} -\alpha_1 \\ -\alpha_2 \\ \vdots \\ -\alpha_N \\ 0 \\ 0 \\ \vdots \\ 0 \\ 0 \\ \alpha_1 p_1 \\ \alpha_2 p_2 \\ \vdots \\ \alpha_N p_N \end{bmatrix}, \quad \mathbf{r}_\mu = \begin{bmatrix} \sum_{j=1}^N \mathcal{P}_{1j} \\ \sum_{j=1}^N \mathcal{P}_{2j} \\ \vdots \\ \sum_{j=1}^N \mathcal{P}_{Nj} \\ 0 \\ 0 \\ \vdots \\ 0 \\ 0 \\ -\sum_{j=1}^N p_{11j} \mathcal{P}_{1j} \\ -\sum_{j=1}^N p_{12j} \mathcal{P}_{2j} \\ \vdots \\ -\sum_{j=1}^N p_{INj} \mathcal{P}_{Nj} \end{bmatrix}, \quad (9b)$$

$$\mathbf{r}_\theta = \begin{bmatrix} 0 \\ 0 \\ \vdots \\ 0 \\ 0 \\ 0 \\ \vdots \\ 0 \\ 0 \\ \sum_{j=1}^N \mathcal{Q}_{1j} \\ \sum_{j=1}^N \mathcal{Q}_{2j} \\ \vdots \\ \sum_{j=1}^N \mathcal{Q}_{Nj} \end{bmatrix}, \quad \mathbf{r}_\nu = \begin{bmatrix} 0 \\ 0 \\ \vdots \\ 0 \\ \mathcal{M} \\ -\mathcal{M} \\ \vdots \\ 0 \\ 0 \\ g_I \mathcal{M} \\ -g_I \mathcal{M} \\ \vdots \\ 0 \end{bmatrix}. \quad (9c)$$

**Table 1:** Constants in the Stiffened Gas Equation of State for water (Le Métayer et al., 2005).

Water phase	Liquid	Vapor
$n$	2.35	1.43
$B$ [GPa]	1	0
$q$ [kJ/kg]	-1167	2030
$\eta$ [kJ/(kg K)]	0	-23.4
$c_v$ [J/(kg K)]	1816	1040
$c_p$ [J/(kg K)]	4267	1487

Equation (8) is solved using the Strang-splitting approach (Strang, 1968; Zein et al., 2010) in two steps/solvers: hyperbolic and relaxation.

### 2.3.1 HYPERBOLIC SOLVER

The homogeneous, hyperbolic system of Eq. (8)

$$\partial_t \mathbf{q} + \nabla \cdot \mathbf{F}(\mathbf{q}) + \mathbf{h}(\mathbf{q}) \nabla \cdot \mathbf{u} = \mathbf{0} \quad (10)$$

is solved for a full-time step,  $\Delta t$ , using the explicit time-marching and flux-splitting approach described in Bryngelson et al. (2020) and Schmidmayer et al. (2020a). The algorithm uses the third-order accurate Total Variation Diminishing (TVD) Runge-Kutta scheme of Gottlieb and Shu (1998) with a fixed time step calculation following the appropriate advective and diffusion numerical constraints. The HLLC approximate Riemann solver (Toro et al., 1994) is used, with proper correction for equations in non-conservative form (Saurel and Abgrall, 1999) in conjunction with the high-order accurate primitive variable WENO reconstruction scheme of Johnsen and Colonius (2006). The divergence term  $\nabla \cdot \mathbf{u}$  is treated using a midpoint rule (Bryngelson et al., 2020).

### 2.3.2 INFINITE RELAXATION SOLVER

An infinite relaxation step at the end of the hyperbolic step updates the phase densities and volume fractions to ensure thermodynamic equilibrium. The Ordinary Differential Equation (ODE) system

$$\partial_t \mathbf{q} = \mathbf{r}_\mu(\mathbf{q}) + \mathbf{r}_\theta(\mathbf{q}) + \mathbf{r}_\nu(\mathbf{q}), \quad (11)$$

where the right-hand-side of Eq. (8) is reduced to a set of ordinary differential equations that ensure thermodynamic equilibrium. The mechanical, thermal, and chemical relaxation terms are activated depending on the model. A sequence of relaxation steps is taken with each model. The characteristic mechanical relaxation time is assumed to be smaller than the heat and chemical characteristic relaxation time (Pelanti and Shyue, 2014).



Here, we briefly discuss the numerical algorithm for each of the different relaxation models, with further details available in the work of (Pelanti and Shyue, 2019).

**$p$ -Relaxation model** Mechanical relaxation is obtained by solving the ODE system

$$\partial_t \mathbf{q} = \mathbf{r}_\mu(\mathbf{q}). \quad (12)$$

The system is solved in the limit of  $\mu_{jk} \rightarrow \infty$  and phase pressures are equal,  $p_k = p$  for all  $k$ . The resulting system informs the quantities that must remain constant through the relaxation step. The initial and final quantity after the relaxation solver, denoted here with superscripts 0 and \*, respectively, are equal. For mechanical relaxation, the following relations hold  $(\rho_k \alpha_k)^0 = (\rho_k \alpha_k)^*$  for all  $k$ ,  $(\rho \mathbf{u})^0 = (\rho \mathbf{u})^*$ ,  $\mathbf{u}^0 = \mathbf{u}^*$ ,  $E^0 = E^*$ , and  $\mathcal{E}^0 = \mathcal{E}^*$ . Manipulating these relations with the SG EoS yields the following iterative algorithm to enforce  $p_k = p$  for all  $k$  and volume fractions  $\alpha_k$  to be updated for mechanical equilibrium. To calculate the volume fraction of phase  $k$ , the volume fraction mixture relation is calculated:  $\alpha_k = (\rho \alpha)_k / \rho_k$ , where  $\rho_k(p_k)$  is the phase density and can be expressed as a function of pressure. Next, the mixture relation,  $\sum_k \frac{(\alpha \rho)_k}{\rho_k(p_k)} = 1$ , is enforced during the relaxation solver. Using the SG EoS, we obtain a relation for the phase density in terms of the mechanical equilibrium pressure (Schmidmayer et al., 2020a),

$$\rho_k(p) = \frac{\gamma_k (p^* + \pi_{\infty k})}{p_k^0 + \gamma_k \pi_{\infty k} + p (\gamma_k - 1)} \rho_k^0. \quad (13)$$

The mechanical equilibrium pressure  $p^*$  is evaluated via iteration. The iteration scheme is a hybrid bisection and Newton-Raphson that is first bracketed to ensure a solution exists (Press et al., 1993). After evaluating the relaxation pressure, the volume fraction for phases  $k = 1, \dots, N$  are evaluated and updated to the state vector. Additionally, the total energy is updated with the relaxation pressure for numerical consistency (Schmidmayer et al., 2020a).

**$pT$ -Relaxation model** For thermal relaxation, the ODE system,

$$\partial_t \mathbf{q} = \mathbf{r}_\mu(\mathbf{q}) + \mathbf{r}_\theta(\mathbf{q}), \quad (14)$$

is solved in the limit of  $\mu_{jk} \rightarrow \infty$ ,  $\theta_{jk} \rightarrow \infty$ , and phase pressures and temperatures are equal,  $p_k = p$  and  $T_k = T$  for all  $k$ , respectively. First, the mechanical relaxation procedure above is performed. Secondly, the ODE system reduces to relations for variables that must hold for thermal relaxation. The same relations as those of mechanical relaxation hold, i.e.,  $(\rho_k \alpha_k)^* = (\rho_k \alpha_k)^{**}$  for all  $k$ ,  $(\rho \mathbf{u})^* = (\rho \mathbf{u})^{**}$ ,  $\mathbf{u}^* = \mathbf{u}^{**}$ ,  $E^* = E^{**}$ , and

$\mathcal{E}^* = \mathcal{E}^{**}$ , with updated superscripts to differentiate from the mechanical relaxation. Using the SG EoS, two algebraic equations are used to find the relaxation pressure and temperature. The mixture relation connecting the pressure and temperature is

$$\sum_k \frac{T^{**} (\rho_k \alpha_k)^* c_{v,k} (n_k - 1)}{p^{**} + B_k} = 1, \quad (15)$$

where the equilibrium temperature is a function of pressure,

$$T^{**}(p^{**}) = \frac{\mathcal{E}^* - \sum_k (\rho_k \alpha_k)^* q_k}{\sum_k (\rho_k \alpha_k)^* c_{v,k} \left( \frac{B_k(n_k-1)}{p^{**} + B_k} + 1 \right)}. \quad (16)$$

The equilibrium pressure and temperature are evaluated using the above hybrid iteration scheme. The volume fraction for  $k = 1, \dots, N$  phases is evaluated as

$$\alpha_k^{**} = \frac{T^{**} (\rho_k \alpha_k)^* c_{v,k} (n_k - 1)}{p^{**} + B_k}, \quad (17)$$

and total energy and updated to the state vector.

**$pTg$ -Relaxation model** Chemical relaxation is obtained by solving the ODE system in Eq. (11). The system is solved in the limit of  $\mu_{jk} \rightarrow \infty$ ,  $\theta_{jk} \rightarrow \infty$ ,  $\nu \rightarrow \infty$ . The phase pressures, temperatures, and Gibbs free energies are equal,  $p_k = p$  and  $T_k = T$  for all  $k$ ,  $g_1 = g_2$ , respectively. Unlike the earlier relaxation models,  $pTg$ -relaxation is activated when the liquid temperature is above the saturation temperature. To calculate the saturation temperature, the liquid and vapor phase Gibbs free energies for the SG EoS are set equal to yield the relation

$$A + \frac{B}{T_{\text{sat}}} + C \ln(T_{\text{sat}}) + D \ln(p_{\text{sat}} + p_{\infty,1}) - \ln(p_{\text{sat}} + p_{\infty,2}) = 0, \quad (18)$$

where

$$A = \frac{c_{p,1} - c_{p,2} + \eta_2 - \eta_1}{c_{p,2} - c_{v,2}}, \quad B = \frac{q_1 - q_2}{c_{p,2} - c_{v,2}},$$

$$C = \frac{c_{p,2} - c_{p,1}}{c_{p,2} - c_{v,2}}, \quad D = \frac{c_{p,1} - c_{v,1}}{c_{p,2} - c_{v,2}}.$$

Given pressure  $p^{**}$  from the  $pT$ -relaxation procedure, the saturation temperature is calculated by finding the root of equation (18) via numerical iteration. If  $T_1 > T_{\text{sat}}$ , then chemical relaxation is activated. Reducing the ODE system yields the relations,  $\rho^{**} = \rho^{\otimes}$ ,  $(\rho \mathbf{u})^{**} = (\rho \mathbf{u})^{\otimes}$ ,  $E^{**} = E^{\otimes}$ , and  $\mathcal{E}^{**} = \mathcal{E}^{\otimes}$ . We note that these relations are different from those of mechanical and thermal relaxation. The superscript  $\otimes$  is the state

after chemical relaxation. We follow the chemical relaxation procedure of [Pelanti and Shyue \(2014\)](#). Using the mixture relations in §2.1 and  $\mathcal{E}_k = \mathcal{E}_k(p_k, \rho_k)$  yields the following quadratic equation for  $T^*$  with coefficients that are functions of  $p^*$ ,

$$a_p (p^*) (T^*)^2 + b_p (p^*) T^* + d_p (p^*) = 0, \quad (19)$$

where

$$\begin{aligned} a_p (p^*) &= \rho^{**} c_{v1} c_{v2} ((n_2 - 1) (p^* + n_1 B_1)) \\ &\quad - \rho^{**} c_{v1} c_{v2} ((n_1 - 1) (p^* + n_2 B_2)), \\ b_p (p^*) &= \mathcal{E}^{**} ((n_1 - 1) c_{v1} (p^* + B_2)) \\ &\quad - \mathcal{E}^{**} ((n_2 - 1) c_{v2} (p^* + B_1)) \\ &\quad + \rho^{**} ((n_2 - 1) c_{v2} \eta_1 (p^* + B_1)) \\ &\quad - \rho^{**} ((n_1 - 1) c_{v1} \eta_2 (p^* + B_2)) \\ &\quad + c_{v2} (p^* + B_1) (p^* + n_2 B_2) \\ &\quad - c_{v1} (p^* + B_2) (p^* + n_1 B_1), \\ d_p (p^*) &= (\eta_2 - \eta_1) (p^* + B_1) (p^* + B_2). \end{aligned}$$

One can solve the quadratic equation for the equilibrium temperature as a function of pressure,

$$T^* = \frac{-b_p (p^*) + \sqrt{(b_p (p^*))^2 - 4a_p (p^*) d_p (p^*)}}{2a_p (p^*)}. \quad (21)$$

The constraint  $g_1 = g_2$  of Eq. (18) is then used to enforce the equilibrium pressure and temperature via numerical iteration. The phase densities and volume fractions are evaluated as

$$\rho_k^* = \frac{p^* + \pi_k}{(\gamma_k - 1) C_{vk} T^*}, \quad \alpha_1^* = \frac{\rho^* - \rho_2^*}{\rho_1^* - \rho_2^*}, \quad (22)$$

and updated to the state vector. Volume fraction  $\alpha_2^*$  can be evaluated using the mixture relation,  $\alpha_2^* = 1 - \alpha_1^* - \sum_{k,j \neq 1,2}^N \alpha_k^{**}$ . Similarly, the mixture density relation calculates the other phase densities.

### 2.3.3 FINITE RELAXATION SOLVER

To verify the implementation of the infinite relaxation solver, we implement a finite relaxation solver for Eq. (11) for a two-phase system with governing equations,

$$\partial_t \alpha_1 + \mathbf{u} \cdot \nabla \alpha_1 = \mathcal{P}_{12} + \mathcal{Q}_{12}/\kappa + \mathcal{M}/\varrho, \quad (23a)$$

$$\partial_t (\alpha_1 \rho_1) + \nabla \cdot (\alpha_1 \rho_1 \mathbf{u}) = \mathcal{M}, \quad (23b)$$

$$\partial_t (\alpha_2 \rho_2) + \nabla \cdot (\alpha_2 \rho_2 \mathbf{u}) = -\mathcal{M}, \quad (23c)$$

$$\partial_t (\alpha_k \rho_k) + \nabla \cdot (\alpha_k \rho_k \mathbf{u}) = 0, \quad k = 1, 2, \quad (23d)$$

$$\partial_t (\rho \mathbf{u}) + \nabla \cdot \left[ \rho \mathbf{u} \otimes \mathbf{u} + \sum_{k=1}^2 \alpha_k p_k \mathbb{I} \right] = 0, \quad (23e)$$

$$\begin{aligned} \partial_t (\alpha_1 \mathcal{E}_1) + \nabla \cdot (\alpha_1 (\mathcal{E}_1 + p_1) \mathbf{u}) &= \\ -p_1 \mathcal{P}_{12} + \mathcal{Q}_{12} + g_1 \mathcal{M}, \end{aligned} \quad (23f)$$

$$\begin{aligned} \partial_t (\alpha_2 \mathcal{E}_2) + \nabla \cdot (\alpha_2 (\mathcal{E}_2 + p_2) \mathbf{u}) &= \\ p_1 \mathcal{P}_{12} - \mathcal{Q}_{12} - g_1 \mathcal{M}. \end{aligned} \quad (23g)$$

Following ([Zein et al., 2010](#)), the interfacial relaxation pressure is  $p_I = \frac{Z_2 p_1 + Z_1 p_2}{Z_1 + Z_2}$  with  $Z_k = \rho_k a_k^2$  as the phase  $k$  acoustic impedance. The other relaxation terms are defined as

$$\kappa = \frac{\frac{p_1 + n_1 B_1}{\alpha_1} + \frac{p_2 + n_2 B_2}{\alpha_2}}{\psi}, \quad (24)$$

where  $\psi = \Gamma_1/\alpha_1 + \Gamma_2/\alpha_2$ , with  $\Gamma_k = n_k - 1$ . The quotient  $\varrho = a/b$  with

$$\begin{aligned} a &= \phi \left( \frac{p_1 + n_1 B_1}{\alpha_1} + \frac{p_2 + n_2 B_2}{\alpha_2} \right) \\ &\quad - \psi \left( \frac{B_1}{\alpha_1 \rho_1 c_{v1}} + \frac{B_2}{\alpha_2 \rho_2 c_{v2}} \right), \end{aligned} \quad (25a)$$

$$\begin{aligned} b &= -\phi \left( \frac{(n_1 - 1) q_1}{\alpha_1} + \frac{(n_2 - 1) q_2}{\alpha_2} \right) + \\ &\quad \psi \left( \frac{e_1 - \frac{B_1}{\rho_1}}{\alpha_1 \rho_1 c_{v1}} + \frac{e_2 - \frac{B_2}{\rho_2}}{\alpha_2 \rho_2 c_{v2}} \right). \end{aligned} \quad (25b)$$

The interfacial equilibrium mass transfer term is

$$\begin{aligned} \varepsilon &= \frac{\left( \frac{e_1 - \frac{B_1}{\rho_1}}{\alpha_1 \rho_1 c_{v1}} + \frac{e_2 - \frac{B_2}{\rho_2}}{\alpha_2 \rho_2 c_{v2}} \right)}{\phi} + \\ &\quad \frac{\left( \frac{B_1}{\alpha_1 \rho_1 c_{v1}} + \frac{B_2}{\alpha_2 \rho_2 c_{v2}} \right)}{\varrho \phi}, \end{aligned} \quad (26)$$

with  $\phi = 1/\alpha_1 \rho_1 c_{v1} + 1/\alpha_2 \rho_2 c_{v2}$ . After solving hyperbolic system, the infinite pressure relaxation model in the previous section is first computed. This step is necessary for other finite relaxation models ([Pelanti, 2021](#)). The right-hand-side of the equation is then computed directly. The relaxation parameters  $\mu_{12}$ ,  $\theta_{12}$ , and  $\nu$  are set to positive finite values. The values are determined heuristically at the highest values that ensured numerical stability of the solver.

## 3 RESULTS & DISCUSSION

### 3.1 TEST PROBLEMS

We verify the MFC implementation of the numerical model using a 1D cavitation problem. We then calculate

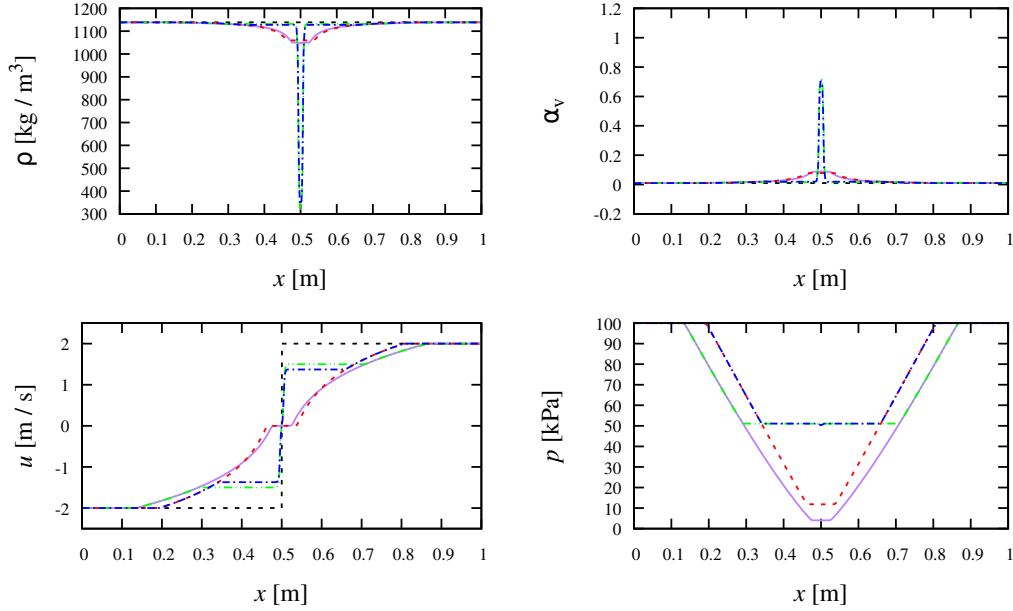


**Figure 1:** Liquid water-water vapor cavitation problem with  $|U| = 2$  m/s at  $t = 3.2$  ms for  $p$  (—),  $p$ - $pT$  (---),  $p$ - $pTg$  (····), and  $p$ - $pT$ - $pTg$  (-·-·) relaxation approach. Dashed black line (- - -): initial condition.

a water shock tube problem with phase change. Exact solutions are not available for these problems. Thus, we compare our results with the numerical solutions of Saurel et al. (2008) and Pelanti and Shyue (2014, 2019) and finite relaxation solver in §2.3.3. We use the material properties of liquid water and water vapor in Table 1. The problems are discretized on a grid using  $N_x = 2000$  numerical cells. The Courant-Friedrichs-Lewy (CFL) condition is kept with a CFL number of 0.9. Non-reflecting boundary conditions (Thompson, 1990) are used at the left and right boundaries.

### 3.1.1 WATER CAVITATION TUBE PROBLEM

We solve a liquid water-water vapor cavitation tube problem (Saurel et al., 2008). The cavitation tube is filled with a mixture of liquid water ( $\rho_l = 1150$  kg/m<sup>3</sup>) and water vapor ( $\rho_g = 0.63$  kg/m<sup>3</sup>) at  $p = 10^5$  Pa. The vapor density was set for initial thermal equilibrium  $T_l = T_v = 354.7$  K. The vapor volume fraction is set to  $\alpha_v = 10^{-2}$  in the domain. The initial  $x$ -direction velocity discontinuity  $|U| = 2$  m/s is set at  $x = 0.5$  m with  $u = -U$  at the left and  $u = +U$  at the right.

Figure 1 shows the cavitation tube problem solution at  $t = 3.2$  ms. The solutions for the  $p$ ,  $p$ - $pT$ ,  $p$ - $pTg$ , and  $p$ - $pT$ - $pTg$  relaxation models are shown and match the results of Pelanti and Shyue (2014). We note that a lower resolution is used in the current simulations compared to Pelanti and Shyue (2014). However, the high-order accurate method in MFC maintained the sharp features of

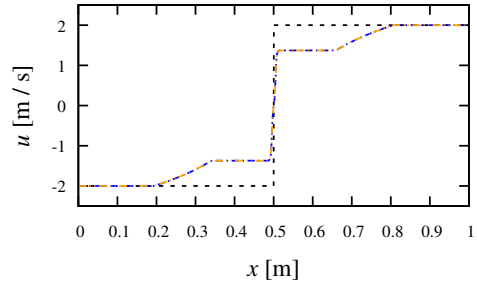


**Figure 2:** Liquid water-water vapor cavitation problem with  $|U| = 2$  m/s at  $t = 3.2$  ms for infinite (---) and finite  $p$ - $pT$ - $pTg$  (-·-·) relaxation. Dashed black line (- - -): initial condition.

the nonlinear waves. For the  $p$ - $pTg$  relaxation model, the  $p$  relaxation is first used followed by the  $pTg$  relaxation model. That is, the  $pT$  relaxation model is not activated. The pair  $p$  and  $p$ - $pT$  infinite relaxation model solutions and pair  $p$ - $pTg$  and  $p$ - $pT$ - $pTg$  infinite relaxation models closely match for density and volume fraction curves. As expected, the chemical relaxation is necessary to see phase change and increase the water vapor volume fraction at  $x = 0.5$  m. Differences between the  $p$ - $pTg$  and  $p$ - $pT$ - $pTg$   $x$ -velocity and pressure relaxation curves are seen at the contact  $x = 0.5$  m and expansion waves. Despite both relaxation models enforcing the chemical equilibrium at the end of each time step, the state variables for the  $pTg$  relaxation in the  $p$ - $pTg$  approach have

the temperature in disequilibrium. Thus, the two different starting points of the  $pTg$  infinite relaxation solver between the relaxation models yield different results.

We now consider the finite relaxation solver presented in §2.3.3 for this problem. The usage of this finite relaxation solver is two-fold: (i) verify the numerical implementation of the infinite relaxation solver and (ii) determine which infinite relaxation solver, between  $pT$ - $pTg$  and  $p$ - $pTg$ , matches the direct numerical simulation. The relaxation parameters in the finite relaxation solver are  $\mu_{12} = 10^8 \cdot 1/\text{Pa}$ ,  $\theta_{12} = 10^8 \cdot \text{Pa/K}$ , and  $\nu = 10^{-3} (\text{kg}^2 \cdot \text{K})/(\text{kJ} \cdot \text{m}^3)$ . Figure 2 shows the matching  $x$ -velocity solutions between the  $pT$ - $pTg$  infinite relaxation solver and finite relaxation solver. The densities, volume fractions, and pressure quantities match both solvers.

### 3.1.2 WATER SHOCK TUBE PROBLEM

The shock tube problem is a Riemann-type problem for the Euler equations and, for a given set of initial conditions, generates three waves: two nonlinear waves (shock or rarefaction) and a linearly degenerate wave known as a contact. For the six-equation model with phase change, Saurel et al. (2008) observed an additional wave develops in the presence of phase change: an evaporation wave. The shock tube problem follows the initial conditions similar to other water (Schmidmayer et al., 2020b) and dodecane (Pelanti and Shyue, 2014) and (Saurel et al., 2008) shock tube problems,

$$(u, p, \alpha_v) = \begin{cases} (0, 10^8, 10^{-8}) & \text{if } x/L \in [0, 0.75], \\ (0, 10^5, 1 - 10^{-8}) & \text{otherwise,} \end{cases} \quad (27)$$

with  $\rho_l = 500 \text{ kg/m}^3$  and  $\rho_v = 50 \text{ kg/m}^3$ .

Figure 3 shows the solution for the water shock tube problem for two different phase relaxation approaches at  $t = 241 \mu\text{s}$ . The  $p$ -relaxation mixture density solution shows the three waves for the Euler-type equations with the rarefaction at approximately  $x = 0.2 \text{ m}$ , contact at  $x = 0.77 \text{ m}$ , and shock at  $x = 0.79 \text{ m}$ . The expected results are achieved for the volume fraction following the material contact at  $x = 0.77 \text{ m}$ . The  $x$ -velocity and pressure solutions show the rarefaction and shock waves. The  $pT$ - $pTg$  relaxation solution is significantly different from the  $p$ -relaxation solution. The shock and contact wave travel further to the right of the domain to  $x = 0.89 \text{ m}$  and  $x = 0.85 \text{ m}$ , respectively. The evaporation wave is at  $x = 0.75 \text{ m}$  and the decrease in water vapor volume fraction from the contact to the evaporation wave. Interestingly, an increase in the  $x$ -velocity and reduction in mixture density occurs in the post-evaporation wave state. A sharp pressure peak is at  $x = 0.75 \text{ m}$  for the  $pT$ - $pTg$  relaxation solution due to the high-order

accurate scheme. The peak diminishes with increasing dissipation, e.g., lowering the CFL number or reducing the high-order accurate scheme to third-order accurate WENO.

## 3.2 UNDEX PROBLEM NEAR AN OBJECT

### 3.2.1 RIGID WALL

We conduct 2D axisymmetric numerical simulations of an underwater bubble explosion problem near an object with phase change using the  $pTg$ -relaxation solver. As illustrated in figure 4, our geometry consists of a flat, rigid, infinitely long wall or object (top). Following Xie et al. (2006) and Pelanti and Shyue (2019), an initially spherical bubble of radius  $R_o$  is placed a distance  $\gamma_o$  from the wall and along the centerline,  $x = 0$ . As a reference, we take  $R_o = 50 \text{ mm}$ . Liquid water of pressure  $p_\infty = 10^5 \text{ Pa}$  and temperature  $T_\infty = 303 \text{ K}$  surrounds the bubble. The bubble is filled with water vapor and a non-condensable ideal gas with a baseline initial pressure  $p_{b,o} = 650 \text{ MPa}$ , density  $\rho_{g,o} = 1400 \text{ kg/m}^3$ , and volume fractions  $\alpha_{vv} = \alpha_{wl} = 10^{-8}$ . The bubble is initialized at a non-dimensional stand-off distance  $\gamma_o = z_o/R_o$ , where  $z_o$  is the initial  $z$ -direction distance from the bubble center to the rigid wall. The growth is due to the resulting pressure difference across the bubble interface. Due to the symmetry in the  $z$ -axis (i.e., the centerline of the domain in Fig. 4), half of the domain is simulated with symmetric boundary conditions. The bottom and right boundary conditions are non-reflecting (Thompson, 1990). The top wall is a rigid, perfectly reflecting, no-slip boundary condition. The simulations use an axisymmetric coordinate system (Meng and Colonius, 2018; Bryngelson et al., 2020). The computational grid is  $580 \times 480$  with domain  $[-0.6, 0.6] \text{ m} \times [-0.7, 0] \text{ m}$ . The CFL condition number is set 0.2.

We conduct a sequence of numerical simulations to investigate the cavitation bubble growth and nearby wall pressure dependence on initial parameters. The parameters are the non-dimensional stand-off distance ( $\gamma_o$ ) and initial bubble gas pressure ( $p_{b,o}$ ). A baseline case for the channel simulations is considered with  $\gamma_o = 3.5$  and  $p_{b,o}^b = 650 \text{ MPa}$ . Two studies are considered: (i) dependence on initial stand-off distance dependence and (ii) driving gas pressure dependence. Simulations with a rigid wall configuration and without the infinite relaxation solver are also computed for comparison. The simulation campaign is summarized in Table 2. Time is non-dimensionalized using the Rayleigh collapse time for a single bubble in a free field,  $t_c = 0.915 R_o \sqrt{\rho_l / \Delta p}$ , where  $\Delta p = p_{b,o}^b - p_{\text{atm}}$  with  $p_{\text{atm}}$  is the atmospheric pressure and the liquid water density  $\rho_l = 1300 \text{ kg/m}^3$ . To compare the maximum wall pressure trends between



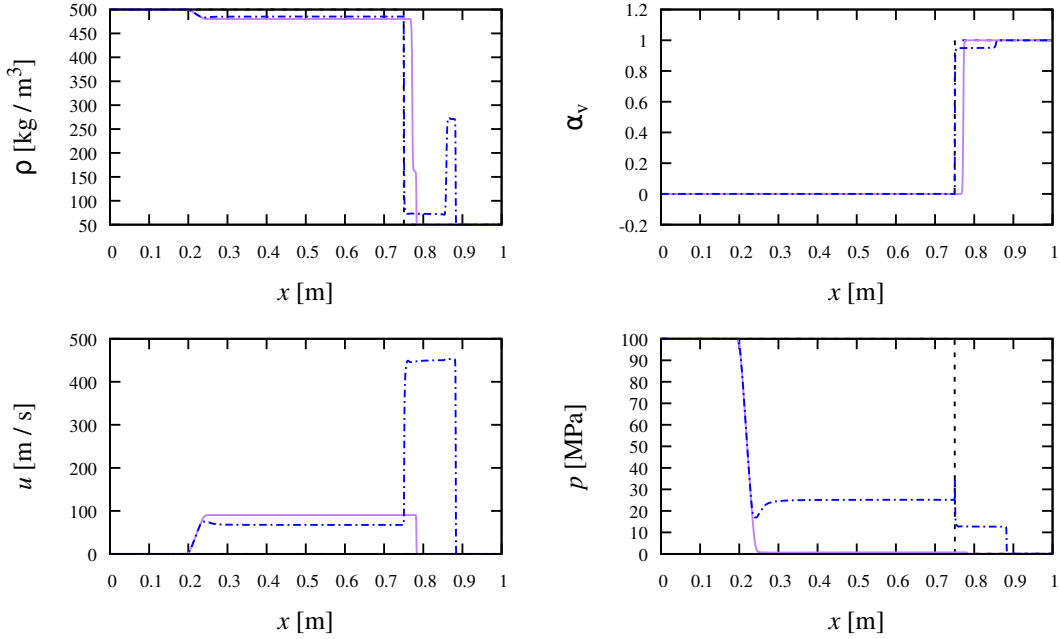


**Figure 3:** Liquid water-water vapor shock tube problem with pressure ratio  $10^3$  at  $t = 241 \mu\text{s}$  for  $p$  (—), and  $p-pT-pTg$  (---) relax implementations. Dashed black line is the initial condition.

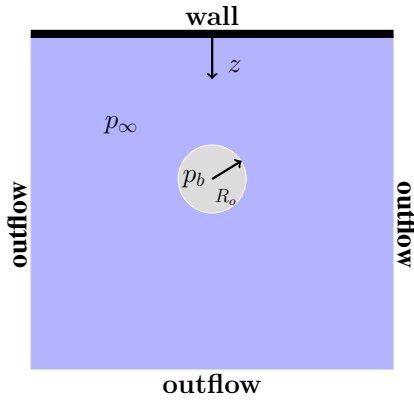


**Figure 4:** Problem schematic of an inertially exploding water vapor and non-condensable gas bubble in a sea of liquid water near a rigid, flat wall.

the two different studies, we use a single dependent variable for the maximum wall pressure, i.e.,

$$p_{w,\max} = f(\gamma_o, p_{b,o}) = g(\gamma_o p_{b,o}^*), \quad (28)$$

where  $p_{w,\max}$  is the non-dimensional bubble pressure and  $p_{b,o}^* = p_{b,o}/p_{b,o}^b$ . The total water vapor mass  $m_{wv}(t/t_c)$  history is non-dimensionalized using the initial total water vapor mass for the baseline simulation.

Figure 5 shows pressure contours for the underwater multiphase bubble explosion problem near a rigid wall for the baseline case. The top contour shows

the instance after the outward propagating, explosion-generated shock impinges on the rigid wall and is reflected towards the bubble with twice the pressure magnitude at  $t = 100 \mu\text{s}$ . The white isoline is the liquid water volume fraction at  $\alpha_{wl} = 0.95$ . Due to the acoustic impedance mismatch between liquid water and the gaseous bubble, the middle contour shows the interaction between the growing bubble and reflected shock produces a rarefaction wave traveling towards and impinging on the rigid wall. The pressure reduction from the rarefaction vaporizes the liquid at the wall and generates a wall-attached bubble (see white isoline of water vapor near the wall in the middle contour). The wall-attached cavitation bubble grows in volume to the reflected rarefaction interaction with the wall. The explosion bubble growth induces the collapse of the wall-attached bubble, which, in turn, produces a shock that impinges on the wall (see right frame). As the cavitation bubble grows, it increases the liquid potential energy. The energy is then transferred to kinetic energy as the liquid collapses the bubble and the bubble impinges on the wall. The shocks and rarefactions continue to propagate outwardly as the explosion bubble grows to its maximum radius and subsequently collapses towards the wall (not shown).

To quantify the pressures produced on the wall from the phase change-induced bubble dynamics, we consider the pressures located at the wall centerline, i.e.,  $(x, z) = (0, 0)$ . Figure 6 shows the centerline wall pressure histories for different initial stand-off distances and

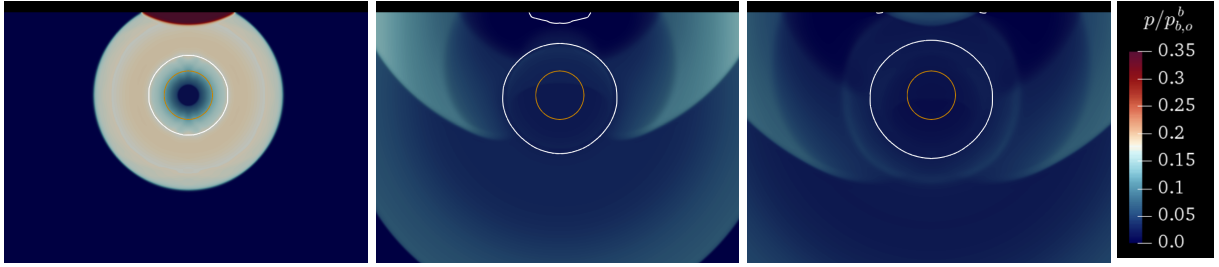


**Figure 5:** Pressure contours of the underwater multiphase bubble explosion problem near a rigid wall with at  $t = 100 \mu s$  (left),  $t = 300 \mu s$  (middle) and  $t = 366 \mu s$  (right) with  $p_{b,o} = 650 \text{ MPa}$  and initial stand-off distance  $\gamma_o = 3.5$ . White contour isoline:  $\alpha_{wl} = 0.9$ . Initial bubble radius interface: (—) with  $R_o = 0.05 \text{ m}$ .

**Table 2:** Initial condition parameters for simulations of the UNDEX problems.

Study	Case #	$\gamma_o$	$p_{b,o} \text{ [GPa]}$
Baseline	1	3.5	0.65
$p_{b,o}$	2-5	3.5	0.300, 0.45, 0.85, 1
$\gamma_o$	6-9	2, 3, 4, 5	0.65

bubble pressures, respectively. As the initial stand-off distance increases, the wall pressure decreases for a constant initial explosion bubble pressure. The maximum wall pressure is experienced at later times as the initial stand-off distance increases. This is expected as the shock travels a longer distance to reach the wall. Moreover, the maximum wall pressure at the wall decays as  $\gamma_o^{-1.13}$ , which has been observed in experiments for underwater explosions (Cole, 1948) and numerical multiphase simulations (Beig et al., 2018; Rodriguez et al., 2021). A later, smaller maximum wall pressure is observed in these cases between  $t/t_c = [0.3, 0.5]$  due to the wall-attached cavitation bubble collapse. Increasing the initial explosion bubble gas pressure for a fixed initial stand-off distance increases the time-synchronized maximum wall pressures linearly (see right frame). The wall-attached cavitation bubble collapse shock impingement occurs between  $t/t_c = [0.4, 0.6]$  that increases with increasing  $p_{b,o}$ . At low enough pressure  $p_{b,o} = 300 \text{ MPa}$ , a cavitation bubble is not generated and does not yield a prominent secondary wall pressure.

Figure 7 shows the maximum wall pressure trends for the explosion and wall-attached cavitation events as a function of initial stand-off distance and bubble pressure. The UNDEX shock trends show expected results. As the product  $\gamma_o p_{b,o}^*$  increases, the maximum wall pressure for the initial stand-off distance study decays as  $\gamma_o^{-1.13}$  (Cole, 1948). The linear maximum pressure increase for the initial bubble pressure is also observed. The wall-attached cavitation bubble collapse maximum

wall pressure is relatively insensitive to the value of initial bubble pressure relative and stand-off distance. The longer duration of the low pressures (i.e., the tail of rarefaction wave) on the wall yields larger wall-attached cavitation bubble growth for higher initial stand-off distances.

Figure 8 shows the mass vapor history of the wall-attached cavitation bubble in the baseline case simulation and different initial stand-off distances. For comparison, the mass vapor history for the  $pT$ -relaxation model is also presented for the baseline case. Without chemical relaxation ( $pT - relax$ ), the water vapor mass linearly decreases during the simulation due to the explosion and shock wave. The same phenomenon is seen in the 1D shock tube problem in figure 3. The baseline case follows the same linear decrease in mass vapor until  $t/t_c = 4$  when the rarefaction wave reflects from the rigid wall. The reduction in pressure at  $t/t_c = 4$  (see figure 6) changes the liquid phase to vapor and increases water vapor mass in the domain. The onset of phase change occurs earliest for stand-off distances  $\gamma_o = 3$  and  $\gamma_o = 3.5$ . For stand-off distances  $\gamma_o < 5$ , the water vapor mass nearly doubles by the end of the simulation at  $t/t_c = 12$  where the rarefaction propagates across the wall, further inducing further cavitation. For  $\gamma_o \geq 5$ , the explosion shock reflected from the bubble and inverts in polarity travels a longer distance to interact with the bubble. As a result, the reflected rarefaction from the acoustic impedance mismatch is weaker and delayed ability to induce phase change at the rigid wall. For the explosion pressure variation study, the stand-off distance is fixed to the baseline value and, thus, the water vapor mass histories are like those of the baseline case shown in figure 6.

### 3.2.2 RIGID WALL WITH COMPLIANT COATING

We now consider similar 2D numerical simulations of an underwater bubble explosion problem with a compliant elastomeric coating attached to the rigid wall. The problem geometry consists of a flat, rigid, infinitely long

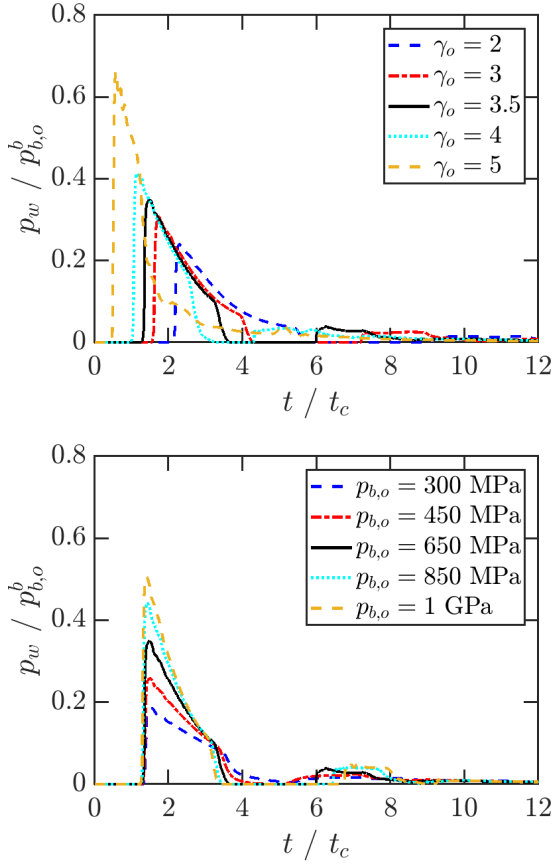


**Figure 6:** Wall pressure histories for different initial stand-off distances (top) and bubble pressures (bottom).

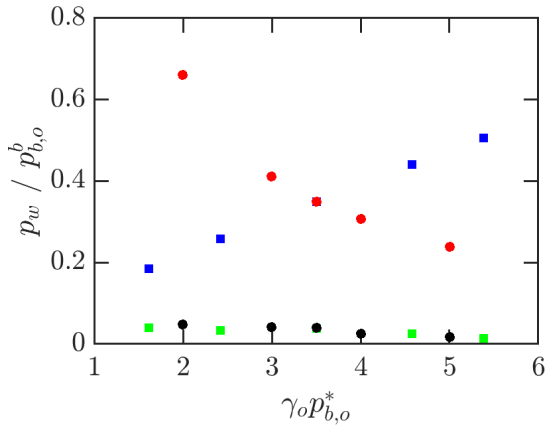


**Figure 7:** Maximum wall pressure scaling trend. The UNDEX shock-generated maximum pressures:  $\gamma_o$  (●) and  $p_{b,o}$  (■) study. Cavitation collapse-generated maximum wall pressure:  $\gamma_o$  (●) and  $p_{b,o}$  (■) study.

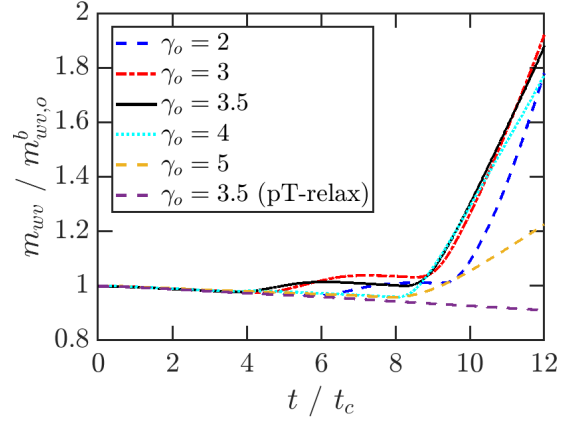


**Figure 8:** Water vapor mass history for underwater bubble explosion problem near a rigid wall for different initial stand-off distances.

wall with an attached elastomeric coating of thickness  $\ell$ , see figure 9. The initially spherical bubble of radius  $R_o$  is placed a distance  $\gamma_o$  from the elastomeric coating and along the centerline,  $x = 0$ . As in §3.2.1, we take  $R_o = 50$  mm. The elastomeric coating has a thickness  $\ell = 2R_o$  and the material properties of polyurea (Amini et al., 2010; Qiao et al., 2011), with density  $\rho_\ell = 1235$  kg/m<sup>3</sup>, speed of sound  $c_\ell = 2030$  m/s. Liquid water of pressure  $p_\infty = 10^5$  Pa and temperature  $T_{\infty,o} = 303$  K surrounds the bubble. The same SG EoS constants as liquid water in Table 1 are used for polyurea. To match the speed of sound of polyurea, the SG EoS constant  $B$  is set to  $B_{\text{polyurea}} = 2.1$  GPa. For simplicity, we neglect the elasticity of the polyurea in this work. However, the interaction between the viscoelasticity and shock-induced bubble collapse near a coating has been previously investigated (Beig et al., 2016) and is readily available within MFC. The bubble is filled with water vapor and a non-condensable ideal gas with the quantities as in the previous section. The initial  $z$ -direction distance  $z_o$  is from the bubble center to the compliant coating for  $\gamma_o = z_o / R_o$ . The same computational boundary conditions as in the previous section are considered here. The grid resolution is kept the same to compare the results between the two different configurations. The simulations have a  $640 \times 480$  computational grid with domain  $[-0.6, 0.6] \text{ m} \times [-0.8, 0] \text{ m}$ . The CFL number is set to 0.1. We consider the same sequence of numerical simulations in Table 2.

We investigate the wave, phase change, and maximum wall pressure dynamics of the UNDEX problem near a wall with a compliant, elastomeric coating. Figure 10 shows pressure contours at three separate times for the UNDEX problem near a compliant object attached to a rigid wall. For comparison, the color contour in figure 5

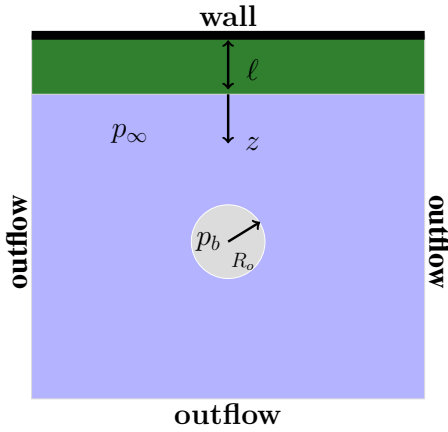


**Figure 9:** Problem schematic of an inertially exploding water vapor and non-condensable gas bubble in a sea of liquid water near an elastomeric coating (polyurea) of thickness  $\ell$  attached to a rigid, flat wall.

is used. The outward propagating shock from the initial condition impinges at the elastomeric coating interface. Due to acoustic impedance mismatch between the coating and liquid water, the explosion shock is partially transmitted into the coating and reflected to the liquid water (see left frame). The transmitted shock impinges on the rigid wall, reflects doubling in pressure, and is mostly transmitted back to the liquid. Both reflected shocks (coating reflected and wall reflected) impinge on the bubble and are reflected and inverted in polarity as rarefactions (see middle frame). The rarefactions interact with the coating (partial transmission and reflection) and wall. However, the rarefactions are weaker in magnitude than the rigid wall-only case in the previous section (see right frame). Simultaneously, the bubble grows, comparable to the rigid wall-only case, and deforms the coating interface. The reduction in the pressure experienced at the wall due to the partial transmission into the coating leads to a decrease in reflected pressure. Figure 11 shows the water vapor mass history for the rigid wall-only baseline,  $pT$  relaxation case, and rigid wall with coating baseline cases. The coating configuration follows the  $pT$  relaxation case, and no significant phase change occurs in the simulation relative to the rigid wall-only case. Thus, the coating inhibits the formation of a sufficiently strong rarefaction wave that induces phase change at the coating interface or rigid wall. In terms of the maximum pressure loading experienced at the rigid wall, figure 12 shows the maximum wall pressures for both the rigid wall and rigid wall with a coating configuration for both the  $\gamma_o$  and  $p_{b,o}$  studies. The acoustic impedance mismatch leads to a fraction of the shock pressure transmitted into the coating and impinging onto the wall. As a result, the maximum wall pressures are lower in coating configu-

ration than the wall-only configuration for both studies. The results are like those observed by Beig et al. (2016) using the hypoelastic model of Rodriguez and Johnsen (2019) for shock-induced bubble collapse problems near a boundary. Future work will investigate UNDEX and bubble collapse problems with a coating with elasticity.

## 4 CONCLUSIONS

We conducted numerical simulations of UNDEX-induced bubble growth near a compliant object (elastomeric coating) with phase change. We use the open-source Multi-component Flow Code (MFC), an Eulerian framework to access these scales and model phase change. The Eulerian six-equation multiphase physical and numerical model uses an interface- and shock-capturing approach. Phase change is modeled as a kinetic process involving volume, thermal, and mass transfer at the material interface. Phase change occurs between the first two phases (e.g., water vapor and liquid water), and infinitely fast pressure and thermal relaxation are assumed for the additional phases. The numerical solver is verified using a 1D cavitation tube problem using the two-phase relaxation solver with finite relaxation. Two axisymmetric UNDEX problems are considered: bubble growth near (i) a rigid wall and (ii) a rigid wall with an elastomeric coating. Due to the acoustic impedance mismatch, the explosion shock reflects from the wall and inverses polarity upon interacting with the bubble. The rarefaction then impinges on the wall, decreases the liquid pressure, and cavitates the liquid water near the wall. The wall-attached cavitation bubble collapses, inducing a secondary increase in pressure on the wall, albeit smaller than the explosion shock. The most water vapor mass production was seen for initial bubble stand-off distances  $2 < \gamma_o < 4$ . For the wall with an elastomeric (polyurea) coating case, the partial reflection and transmission of the explosion shock inhibit an intense pressure inversion of the reflected shock with the bubble. Thus, the rarefaction interaction with either the coating or rigid wall did not lead to phase change irrespective of the initial bubble pressure or stand-off distance from the coating. Future studies will investigate UNDEX wall- and coating-attached cavitation bubbles with phase change and elasticity.

## ACKNOWLEDGEMENTS

This work was supported in part by the ONR Grant No. N00014-18-1-2625 (under Dr. Timothy Bentley).

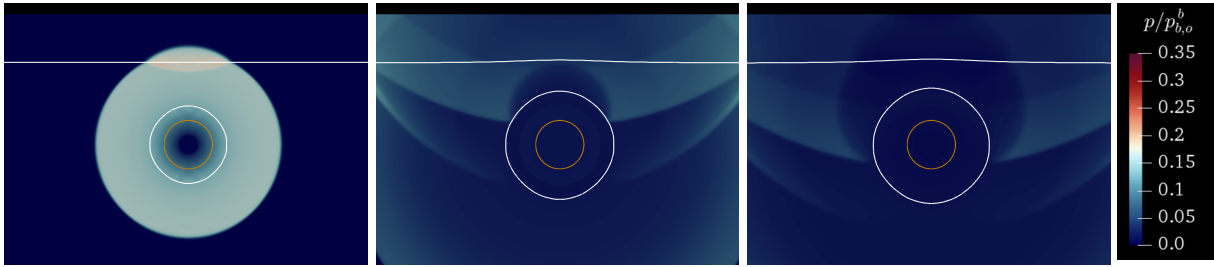


**Figure 10:** Pressure contours of the underwater multiphase bubble explosion problem near an elastomeric coating with at  $t = 100 \mu s$  (left),  $t = 300 \mu s$  (middle) and  $t = 366 \mu s$  (right) with  $p_{b,o} = 650 \text{ MPa}$  and initial stand-off distance  $\gamma_o = 3.5$ . White contour isoline:  $\alpha_{wl} = 0.9$ . Initial bubble radius interface: (—) with  $R_o = 0.05 \text{ m}$ .

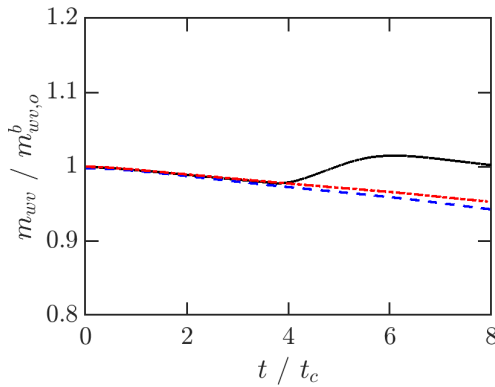


**Figure 11:** Water vapor mass history for underwater bubble explosion problem near a rigid wall and compliant coating. Baseline wall case (—), baseline wall case with no phase change (---), and baseline compliant coating case (-.-.-).

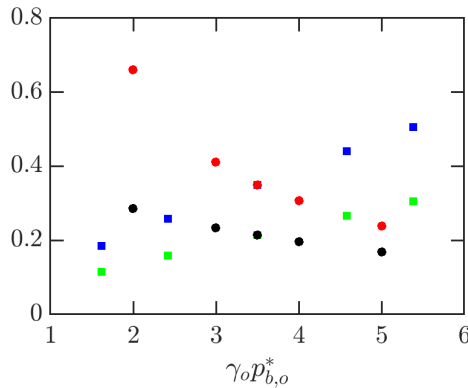


**Figure 12:** Maximum wall pressure scaling trend. UNDEX shock-generated maximum pressures near a wall:  $\gamma_o$  (●) and  $p_{b,o}$  (■) study. Maximum pressures for a wall with a coating:  $\gamma_o$  (●) and  $p_{b,o}$  (■) study.

## REFERENCES

- R. Abgrall, How to Prevent Pressure Oscillations in Multicomponent Flow Calculations: A Quasi Conservative Approach, *J. Comput. Phys.* 125 (1996) 150–160.
- A. A. Aganin, M. A. Ilgamov, L. A. Kosolapova, V. G. Malakhov, Dynamics of a cavitation bubble near a solid wall, *Thermophys. Aeromechanics* 23 (2016) 211–220.
- G. Allaire, S. Clerc, S. Kokh, A Five-Equation Model for the Simulation of Interfaces between Compressible Fluids, *J. Comput. Phys.* 181 (2002) 577–616.
- M. R. Amini, J. Simon, S. Nemat-Nasser, Numerical modeling of effect of polyurea on response of steel plates to impulsive loads in direct pressure-pulse experiments, *Mech. Mater.* 42 (2010) 615–627.
- M. Baer, J. Nunziato, A two-phase mixture theory for the deflagration-to-detonation transition (ddt) in reactive granular materials, *Int. J. Multiph. Flow* 12 (1986) 861–889.
- S. A. Beig, E. Johnsen, Maintaining interface equilibrium conditions in compressible multiphase flows using interface capturing, *J. Comput. Phys.* 302 (2015) 548–566.
- S. A. Beig, M. Rodriguez, E. Johnsen, Non-spherical bubble collapse near rigid and compliant surfaces, in: 31st Symp. Nav. Hydrodyn., 2016, pp. 1–15.
- S. A. Beig, B. Aboulhasanzadeh, E. Johnsen, Temperatures produced by inertially collapsing bubbles near rigid surfaces, *J. Fluid Mech.* 852 (2018) 105–125.
- T. B. Benjamin, A. T. Ellis, The Collapse of Cavitation Bubbles and the Pressures thereby Produced against Solid Boundaries, *Philos. Trans. R. Soc. A Math. Phys. Eng. Sci.* 260 (1966) 221–240.



- J. R. Blake, D. C. Gibson, Cavitation Bubbles Near Boundaries, Annu. Rev. Fluid Mech. 19 (1987) 99–123.
- J. R. Blake, B. B. Taib, G. Doherty, Transient cavities near boundaries. Part 1. Rigid boundary, J. Fluid Mech. 170 (1986) 479–497.
- E. A. Brujan, H. Takahira, T. Ogasawara, Planar jets in collapsing cavitation bubbles, Exp. Therm. Fluid Sci. 101 (2019) 48–61.
- S. H. Bryngelson, K. Schmidmayer, V. Coralic, J. C. Meng, K. Maeda, T. Colonius, MFC: An open-source high-order multi-component, multi-phase, and multi-scale compressible flow solver, Comput. Phys. Commun. (2020) 107396.
- R. H. Cole, Underwater explosions., Princeton, 1948.
- V. Coralic, T. Colonius, Shock-induced collapse of a bubble inside a deformable vessel, Eur. J. Mech. - B/Fluids 40 (2013) 64–74.
- J.-P. Franc, M. Riondet, A. Karimi, G. L. Chahine, Impact Load Measurements in an Erosive Cavitating Flow, J. Fluids Eng. 133 (2011) 1–8.
- S. Gottlieb, C.-W. Shu, Total variation diminishing Runge-Kutta schemes, Math. Comput. Am. Math. Soc. 67 (1998) 73–85.
- F. H. Harlow, A. A. Amsden, Fluid Dynamics, Monograph LA-4700, Los Alamos, NM, 1971.
- C.-T. Hsiao, A. Jayaprakash, A. Kapahi, J.-K. Choi, G. L. Chahine, Modelling of material pitting from cavitation bubble collapse, J. Fluid Mech. 755 (2014) 142–175.
- G.-S. Jiang, C.-W. Shu, Efficient Implementation of Weighted ENO Schemes, J. Comput. Phys. 126 (1996) 202–228.
- E. Johnsen, T. Colonius, Implementation of WENO schemes in compressible multicomponent flow problems, J. Comput. Phys. 219 (2006) 715–732.
- E. Johnsen, T. Colonius, Numerical simulations of non-spherical bubble collapse, J. Fluid Mech. 629 (2009) 231–262.
- A. K. Kapila, R. Menikoff, J. B. Bdzil, S. F. Son, D. S. Stewart, Two-phase modeling of deflagration-to-detonation transition in granular materials: Reduced equations, Phys. Fluids 13 (2001) 3002–3024.
- K.-H. Kim, G. Chahine, J.-P. Franc, A. Karimi (Eds.), Advanced Experimental and Numerical Techniques for Cavitation Erosion Prediction, volume 106 of *Fluid Mechanics and Its Applications*, Dordrecht, 2014.
- M. Kornfeld, L. Suvorov, On the destructive action of cavitation, J. Appl. Phys. 15 (1944) 495–506.
- W. Lauterborn, H. Bolle, Experimental investigations of cavitation-bubble collapse in the neighbourhood of a solid boundary, J. Fluid Mech. 72 (1975) 391.
- O. Le Métayer, J. Massoni, R. Saurel, Élaboration des lois d'état d'un liquide et de sa vapeur pour les modèles d'écoulements diphasiques, Int. J. Therm. Sci. 43 (2004) 265–276.
- O. Le Métayer, J. Massoni, R. Saurel, Modelling evaporation fronts with reactive Riemann solvers, J. Comput. Phys. 205 (2005) 567–610.
- J. C. Meng, T. Colonius, Numerical simulation of the aerobreakup of a water droplet, J. Fluid Mech. 835 (2018) 1108–1135.
- L. Molefe, I. R. Peters, Jet direction in bubble collapse within rectangular and triangular channels, Phys. Rev. E 100 (2019) 063105–1–9.
- A. Murrone, H. Guillard, A five equation reduced model for compressible two phase flow problems, J. Comput. Phys. 202 (2005) 664–698.
- C. F. Naude', A. T. Ellis, On the Mechanism of Cavitation Damage by Nonhemispherical Cavities Collapsing in Contact With a Solid Boundary, J. Basic Eng. 83 (1961) 648–656.
- V. T. Nguyen, T. H. Phan, W. G. Park, Numerical modeling of multiphase compressible flows with the presence of shock waves using an interface-sharpening five-equation model, Int. J. Multiph. Flow 135 (2021) 103542–1–22.
- M. Pelanti, K. M. Shyue, A mixture-energy-consistent six-equation two-phase numerical model for fluids with interfaces, cavitation and evaporation waves, J. Comput. Phys. 259 (2014) 331–357.
- M. Pelanti, K.-M. Shyue, A numerical model for multiphase liquid–vapor–gas flows with interfaces and cavitation, Int. J. Multiph. Flow 113 (2019) 208–230.
- M. Pelanti, Arbitrary-rate relaxation techniques for the numerical modeling of compressible two-phase flows with heat and mass transfer, arXiv:2108.00556 (2021).
- G. Perigaud, R. Saurel, A compressible flow model with capillary effects, J. Comput. Phys. 209 (2005) 139–178.

- T.-H. Phan, V.-T. Nguyen, T.-N. Duy, D.-H. Kim, W.-G. Park, Numerical study on simultaneous thermodynamic and hydrodynamic mechanisms of underwater explosion, Int. J. Heat Mass Transf. 178 (2021) 121581.
- M. S. Plesset, R. B. Chapman, Collapse of an initially spherical vapour cavity in the neighbourhood of a solid boundary, J. Fluid Mech. 47 (1971) 283–290.
- W. H. Press, S. A. Teukolsky, W. T. Vetterling, B. P. Flannery, *Numerical Recipes in FORTRAN; The Art of Scientific Computing*, 2nd ed., Cambridge University Press, USA, 1993.
- J. Qiao, A. V. Amirkhizi, K. Schaaf, S. Nemat-Nasser, G. Wu, Dynamic mechanical and ultrasonic properties of polyurea, Mech. Mater. 43 (2011) 598–607.
- L. Rayleigh, On the Pressure developed in a Liquid during the Collapse of a Spherical Cavity, Philos. Mag. 6 (1917) 94–98.
- M. Rodriguez, E. Johnsen, A high-order accurate five-equations compressible multiphase approach for viscoelastic fluids and solids with relaxation and elasticity, J. Comput. Phys. 379 (2019) 70–90.
- M. Rodriguez, S. A. Beig, C. N. Barbier, E. Johnsen, Dynamics of an inertially collapsing gas bubble between two parallel, rigid walls, J. Fluid Mech. Submitted (2021).
- M. Rodriguez, Numerical Simulations of Bubble Dynamics Near Viscoelastic Media, Ph.D. thesis, University of Michigan, 2018.
- R. Saurel, R. Abgrall, A Simple Method for Compressible Multifluid Flows, SIAM J. Sci. Comput. 21 (1999) 1115–1145.
- R. Saurel, F. Petitpas, R. Abgrall, Modelling phase transition in metastable liquids: application to cavitating and flashing flows, J. Fluid Mech. 607 (2008) 313–350.
- R. Saurel, F. Petitpas, R. A. Berry, Simple and efficient relaxation methods for interfaces separating compressible fluids, cavitating flows and shocks in multiphase mixtures, J. Comput. Phys. 228 (2009) 1678–1712.
- K. Schmidmayer, S. H. Bryngelson, T. Colonius, An assessment of multicomponent flow models and interface capturing schemes for spherical bubble dynamics, J. Comput. Phys. 402 (2020a) 109080.
- K. Schmidmayer, F. Petitpas, S. Le Martelot, E. Daniel, ECOGEN: An open-source tool for multiphase, compressible, multiphysics flows, Comput. Phys. Commun. 251 (2020b) 107093.
- R. K. Shukla, C. Pantano, J. B. Freund, An interface capturing method for the simulation of multi-phase compressible flows, J. Comput. Phys. 229 (2010) 7411–7439.
- K.-M. Shyue, An Efficient Shock-Capturing Algorithm for Compressible Multicomponent Problems, J. Comput. Phys. 142 (1998) 208–242.
- G. Strang, On the Construction and Comparison of Difference Schemes, SIAM J. Numer. Anal. 5 (1968) 506–517.
- O. Supponen, D. Obreschkow, M. Tinguely, P. Kobel, N. Dorsaz, M. Farhat, Scaling laws for jets of single cavitation bubbles, J. Fluid Mech. 802 (2016) 263–293.
- O. Supponen, D. Obreschkow, P. Kobel, M. Tinguely, N. Dorsaz, M. Farhat, Shock waves from nonspherical cavitation bubbles, Phys. Rev. Fluids 2 (2017) 093601–1–20.
- K. W. Thompson, Time-dependent boundary conditions for hyperbolic systems, II, J. Comput. Phys. 89 (1990) 439–461.
- A. Tiwari, J. B. Freund, C. Pantano, A diffuse interface model with immiscibility preservation, J. Comput. Phys. 252 (2013) 290–309.
- Y. Tomita, A. Shima, Mechanisms of impulsive pressure generation and damage pit formation by bubble collapse, J. Fluid Mech. 169 (1986) 535.
- E. F. Toro, M. Spruce, W. Speares, Restoration of the contact surface in the HLL-Riemann solver, Shock Waves 4 (1994) 25–34.
- T. Trummer, S. H. Bryngelson, K. Schmidmayer, S. J. Schmidt, T. Colonius, N. A. Adams, Near-surface dynamics of a gas bubble collapsing above a crevice, J. Fluid Mech. 899 (2020) A16.
- W. Xie, T. Liu, B. Khoo, Application of a one-fluid model for large scale homogeneous unsteady cavitation: The modified Schmidt model, Comput. Fluids 35 (2006) 1177–1192.
- A. Zein, M. Hantke, G. Warnecke, Modeling phase transition for compressible two-phase flows applied to metastable liquids, J. Comput. Phys. 229 (2010) 2964–2998.